Introduction

In reservoir engineering or CO_2 geological storage, a proper well modeling is required to simulate accurately multiphase flow. An efficient method must take into account important well parameters such as the singular pressure distribution in the well vicinity and the large difference of scales between the wellbore radius and the reservoir dimension. Current methods are based on single-phase near-well analytical solutions and well indexes developed in the papers of Peaceman (1978, 1983). Despite the assumptions of 2D uniform rectangular grids in homogeneous media, Peaceman's approach is widely used in reservoir simulation. However, this approach cannot be used in order to take accurately into account heterogeneities. This is in particular the case for deviated wells and stratified heterogeneities. For this reason a specific model is needed. This work addresses the 3D numerical simulation of multiphase flow in near-well regions.

The near-well model proposed in this paper is based on 3D meshes that are refined around the well and on the use of accurate finite volume schemes. The first step of the discretization is to create a radial mesh that is exponentially refined down to the well boundary. This radial local refinement implies to build a matching mesh between the radial grid and the reservoir CPG grid using either hexahedra or both tetrahedra and pyramids as seen in Figure 1. This transition zone enables to couple the near-well simulation and a global reservoir simulation.

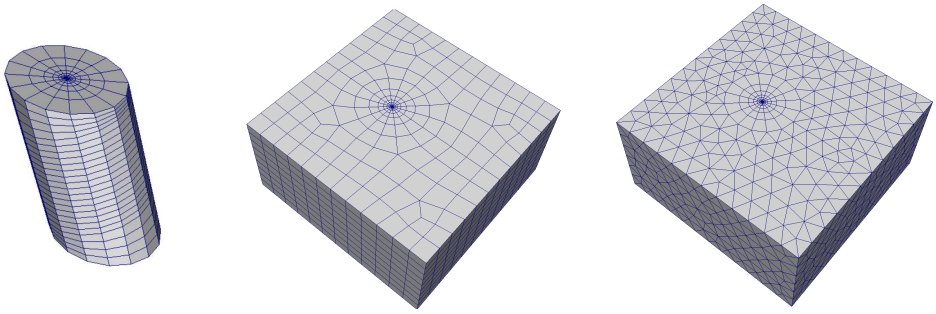

(a) exponentially refined radial mesh

(b) unstructured mesh with only hexahedra

(c) hybrid mesh with hexahedra, tetrahedra and pyramids

Figure 1 *Near-well meshes*

Due to the complex geometry, multiphase flow simulations with such kind of meshes require multipoint flux approximation schemes (MPFA). In this framework, various MPFA methods are used, namely the O, L, G and GradCell schemes. The O and L methods are widely used in the oil industry for the discretization of Darcy fluxes in multiphase porous media flow models, see for example Aavatsmark (2002, 2007); Aavatsmark et al. (2008); Agélas and Masson (2008); Edwards (2002); Edwards and Rogers (1998) and references therein. The G and GradCell schemes are newer methods, detailed in Agélas et al. (2010a,b) and briefly described in the next section. The G scheme is an extension of the L scheme. It uses, as the O and L schemes, a flux formulation based on the construction of a subcell gradient around each vertex satisfying flux and potential continuity conditions. The construction of the GradCell scheme rather starts from a non symmetric discrete variational formulation based on two cellwise constant gradients. The first gradient is consistent and the second gradient satisfies a weak convergence property. Both the O, L, G and the GradCell schemes are compact in the sense that they have a sparse stencil, typically at most 27 points for topologically Cartesian meshes. Unfortunately their non symmetry leads to a conditional coercivity depending, for general polyhedral meshes, both on the distorsion of the mesh and on the permeability tensor.

The SUSHI scheme (Scheme Using Stabilization and Hybrid Interfaces) introduced in Eymard et al. (2009) is a symmetric version of the GradCell scheme using only the consistent gradient in the discrete variational formulation. It leads to an unconditionally coercive scheme, but this is at the expense of the

sparsity of the stencil which is typically between twice and three times larger than the GradCell scheme stencil.

These remarks motivate the introduction of a new SUSHI scheme (Scheme Using Stabilization and Harmonic Interfaces) which combines ideas of both the O scheme and of the previous SUSHI scheme in order to achieve both the sparsity of the stencil and the symmetry of the scheme. This is the first objective of this paper.

Our second objective is to study the behavior of different families of MPFA schemes on near-well simulations using the two types of meshes plotted in Figure 1. Previous simulations have been performed by Mundal et al. (2008, 2009) for single-phase Darcy flow on 2D grids. Our work extends this study to multiphase flow on 3D grids. We first compare the O, L, G, GradCell and SUSHI schemes for the deviated well single-phase Darcy flow analytical solution described in Aavatsmark and Klausen (2003) with an homogeneous anisotropic permeability tensor. Then, a CO_2 injection near-well simulation is performed using a two-phase water gas Darcy flow model with solubility of the CO_2 component in the water phase. The results obtained for the two types of meshes are compared using the MPFA O scheme in terms of space convergence.

Finite volume schemes

Let $\Omega \subset \mathbb{R}^d$ be a bounded polygonal domain of $\mathbb{R}^d$ and Λ be a symmetric positive definite tensor field, the following model problem is considered for a right hand side $f \in L^2(\Omega)$: find $\bar{u} \in H_0^1(\Omega)$ (the potential) such that

$$-\nabla \cdot (\Lambda \nabla \bar{u}) = f \text{ in } \Omega. \tag{1}$$

Let $\mathcal{D} = \left(\mathcal{T}, \mathcal{E}, \mathcal{P}\right)$ be an admissible finite volume discretization of Ω where $\mathcal{T}$ is the set of cells K, $\mathcal{E} = \mathcal{E}^i \cup \mathcal{E}^b$ is the set of faces σ with $\mathcal{E}^i$ the set of inner faces and $\mathcal{E}^b$ the set of boundary faces, and $\mathcal{P}$ is the set of cell centers $\boldsymbol{x}_K \in K$.

We denote by $\mathcal{E}_K$ the set of faces σ of the cell K, by $n_{K,\sigma}$ their unit normal vectors outward to the cell K, and by $d_{K,\sigma}$ the distance between the cell center $\boldsymbol{x}_K$ and the face σ. Let m_K be the volume of the cell K and Λ_K be the mean value $\frac{1}{m_K}\int_K \Lambda(x)\, d\boldsymbol{x}$. We also denote by m_σ the surface of the face σ and by x_σ the center of gravity of the face σ.

Let $X_\mathcal{T}$ be the set of cellwise constant functions such that for any $u \in X_\mathcal{T}$ we have $u(x) = u_K$ for all $x \in K$. A finite volume scheme builds a conservative approximation $F_{K,\sigma}(u)$ of the normal fluxes $\displaystyle\int_\sigma \Lambda \nabla \bar{u} \cdot n_{K,\sigma}\, d\sigma$ such that $F_{K,\sigma}(u) + F_{L,\sigma}(u) = 0$ for all faces $\sigma \in \mathcal{E}_K \cap \mathcal{E}_L$. Then, $\bar{u}$ is approximated by the discrete solution u of the linear system

$$\sum_{\sigma \in \mathcal{E}_K} F_{K,\sigma}(u) = -\int_K f\, d\boldsymbol{x}, \text{ for all } K \in \mathcal{T}. \tag{2}$$

The two keys properties to obtain the convergence of u to $\bar{u}$ are the consistency of the numerical fluxes $F_{K,\sigma}(u)$ and the coercivity of the bilinear form $\langle ., . \rangle_\mathcal{D}$ defined on $X_\mathcal{T} \times X_\mathcal{T}$ by

$$\langle u, v \rangle_\mathcal{D} = \sum_{\sigma = \mathcal{E}_K \cap \mathcal{E}_L \in \mathcal{E}^i} F_{K,\sigma}(u)(v_L - v_K) - \sum_{K \in \mathcal{T}} \sum_{\sigma \in \mathcal{E}_K \cap \mathcal{E}^b} F_{K,\sigma}(u) v_K, \tag{3}$$

such that the finite volume scheme (2) is equivalent to the variational formulation

$$\text{find } u \in X_\mathcal{T} \text{ such that } \langle u, v \rangle_\mathcal{D} = \int_\Omega f v\, d\boldsymbol{x},\ \forall v \in X_\mathcal{T}. \tag{4}$$

We refer to Agélas et al. (2010a) for the rigorous framework and a detailed proof of convergence for piecewise smooth permeability tensors and minimal regularity solutions $\bar{u}$.

As shown below, the G and GradCell schemes (as well as the O and L schemes), lead to a non symmetric bilinear form $\langle ., . \rangle_{\mathcal{D}}$ which results in a mesh and permeability tensor dependent coercivity. This is not the case of the new SUSHI scheme presented in this paper which is by construction symmetric and hence unconditionally coercive while preserving the same stencil as the O scheme.

The G scheme

The G method described in Agélas et al. (2010a) is an extension of the MPFA L scheme introduced by Aavatsmark et al. (2007, 2008). Its contruction is recalled below. Let us first define the family $\mathcal{G}$ of all possible face groups such that $G \in \mathcal{G}$ is a set of d faces σ of a given cell K sharing a given vertex s of K. For each G in $\mathcal{G}$, let $\mathcal{T}_G$ be the group of cells L such that $\mathcal{E}_L \cap G \neq \emptyset$ (see the example on Figure 2(a) with $G = \{\sigma, \sigma'\}$ and $\mathcal{T}_G = \{K, L_1, L_2\}$). Given $u \in X_{\mathcal{T}}$ and a given group G, a cellwise constant

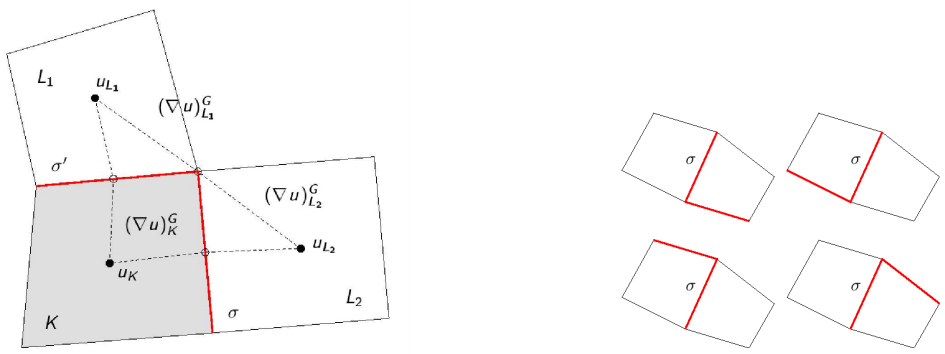

(a) cellwise constant gradient reconstruction for a given group $G = \{\sigma, \sigma'\}$

(b) example of set $\mathcal{G}_\sigma$ for a given σ

Figure 2 *Example of notations for the G scheme*

gradient reconstruction $(\nabla_{\mathcal{D}} u)^G_L$ is obtained on each cell $L \in \mathcal{T}_G$ using a piecewise linear interpolation of the potential on each cell L of $\mathcal{T}_G$ satisfying potential and normal fluxes continuity at the faces $\sigma \in G$. In practice, it amounts to solve a local linear system for the vector $(\nabla_{\mathcal{D}} u)^G_K$, for a specific cell K of $\mathcal{T}_G$

$$A^G (\nabla_{\mathcal{D}} u)^G_K = B^G, \tag{5}$$

assuming that the matrix A^G is nonsingular. The gradients $(\nabla_{\mathcal{D}} u)^G_L$ for the remaining cells L of $\mathcal{T}_G$ are readily deduced from $(\nabla_{\mathcal{D}} u)^G_K$. Then, the following conservative and consistent subfluxes

$$F^G_{L,\sigma}(u) = m_\sigma \Lambda_L (\nabla_{\mathcal{D}} u)^G_L \cdot n_{L,\sigma}, \tag{6}$$

are defined for all $L \in \mathcal{T}_G$. The numerical flux $F_{K,\sigma}(u)$ is a convex linear combination of the subfluxes $F^G_{K,\sigma}(u)$ over the set $\mathcal{G}_\sigma$ of all possible groups G containing the face σ (see the example on Figure 2(b))

$$F_{K,\sigma}(u) = \sum_{G \in \mathcal{G}_\sigma} \theta^G_\sigma \, F^G_{K,\sigma}(u). \tag{7}$$

Different strategies can be applied to compute the weights θ^G_σ. On one hand, the L scheme is obtained by choosing a single group G for each face σ and each vertex $s \in \sigma$ and by setting the fixed weights $\theta^G_\sigma = \frac{1}{N_s}$ where N_s is the number of vertices of the face σ. The choice of the group G is done to enhance the monotonicity of the scheme (see Aavatsmark et al. (2007, 2008)). On the other hand, the G scheme keeps all the possible groups G and the weights θ^G_σ are adapted to enhance the coercivity of the scheme according to a local criterion (see Agélas et al. (2010a)).

The GradCell scheme

The construction of the GradCell scheme described in Agélas et al. (2010b) starts from the variational formulation (4) using two cellwise constant gradient reconstructions and a stabilization by residuals to define the bilinear form $\langle ., . \rangle_{\mathcal{D}}$ on $X_{\mathcal{T}} \times X_{\mathcal{T}}$

$$\langle u, v \rangle_{\mathcal{D}} = \sum_{K \in \mathcal{T}} m_K \Lambda_K (\nabla_{\mathcal{D}} u)_K \cdot (\widetilde{\nabla}_{\mathcal{D}} v)_K \; + \sum_{K \in \mathcal{T}} \sum_{\sigma \in \mathcal{E}_K} \frac{m_\sigma}{d_{K,\sigma}} R_{K,\sigma}(u) R_{K,\sigma}(v).$$

The cellwise constant gradients are obtained via the Green formula and trace reconstructions

$$\begin{cases} (\widetilde{\nabla}_{\mathcal{D}} v)_K = \frac{1}{m_K} \sum_{\sigma \in \mathcal{E}_K} m_\sigma \Big(\gamma_\sigma(v) - v_K \Big) n_{K,\sigma}, \\ (\nabla_{\mathcal{D}} v)_K = \frac{1}{m_K} \sum_{\sigma \in \mathcal{E}_K} m_\sigma \Big(I_{K,\sigma}(v) - v_K \Big) n_{K,\sigma}. \end{cases}$$

The linear interpolation $\gamma_\sigma(v)$ at the face center $\boldsymbol{x}_\sigma$ uses only the two neighboring cells v_K and v_L of the face σ, and $I_{K,\sigma}(v)$ is a consistent linear interpolation at the face center $\boldsymbol{x}_\sigma$ using only cells sharing a face with K. The residuals are defined by

$$R_{K,\sigma}(v) = I_{K,\sigma}(v) - v_K - (\nabla_{\mathcal{D}} v)_K \cdot (\boldsymbol{x}_\sigma - \boldsymbol{x}_K).$$

The conservative numerical fluxes are deduced from the definition of the bilinear form (3). It leads to a scheme stencil using the neighbors of the neighbors of a given cell K (see Figure 3). For a topologically Cartesian mesh it leads to a 21 points stencil in 3D compared with a 27 points stencil for the O scheme. For simplicial meshes the stencil is even more reduced compared with the O scheme.

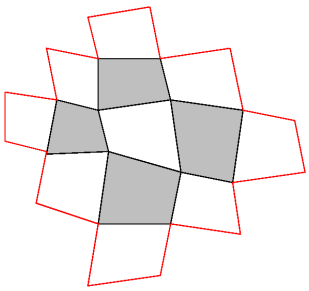

Figure 3 *GradCell stencil on a 2D topologically Cartesian mesh*

The SUSHI scheme

We present here a 3D compact-stencil version of the SUSHI scheme first described in Eymard et al. (2009) and presented in the case of 2D diffusion problems in Agélas et al. (2009). This new version of the scheme, also named SUSHI (Scheme Using Stabilization and Harmonic Interfaces) gathers the advantages of the SUSHI scheme presented in Eymard et al. (2009), and that of compact-stencil schemes such as MPFA O scheme, since it preserves a 27 points stencil in the case of hexahedral structured meshes. The simulation domain is first gridded by general polyhedrical control volumes (Figure 4 shows an example of a general hexahedron, and the notations used below). Then a submesh is based on the following procedure:

1. for each control volume $K \in \mathcal{T}$, we choose a point denoted by $\boldsymbol{x}_K$, called the center of the control volume, at which the unknown will be approximated;
2. at each face σ (even non planar), a point, denoted by $\boldsymbol{y}_\sigma$ is chosen following the harmonic method presented in Agélas et al. (2009): this method allows to express the value at $\boldsymbol{y}_\sigma$ by a consistent linear combination of the values at the points $\boldsymbol{x}_K$ and $\boldsymbol{x}_L$, the centers of the control volumes K and L such that σ is the interface between K and L;

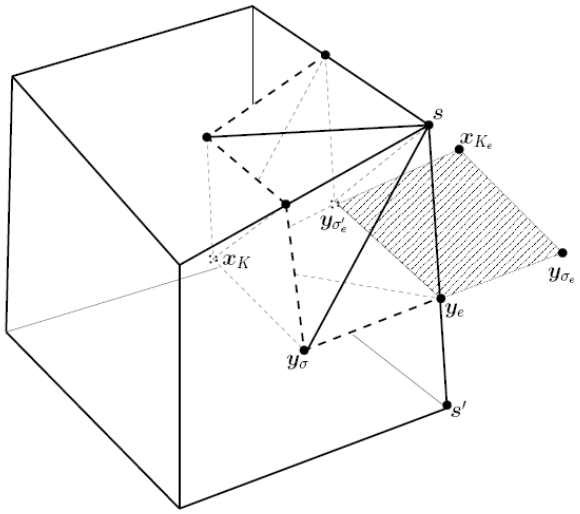

Figure 4 *Construction of the submesh $M_{K,\boldsymbol{s}}$ of a control volume*

3. at each edge e of the mesh, a point, denoted by $\boldsymbol{y}_e$, is chosen such that the value at $\boldsymbol{y}_e$ can be expressed by a linear combination of the values at the points $\boldsymbol{y}_{\sigma_e}$, $\boldsymbol{y}_{\sigma'_e}$ and $\boldsymbol{x}_{K_e}$, where e is a common edge of the faces σ_e and σ'_e, both of them being faces of the same control volume K_e;

4. the subcontrol volume $K_{\boldsymbol{s}}$ is given, for each control volume K and each vertex of K, denoted by $\boldsymbol{s} \in \mathcal{V}_K$, as the polyhedron with vertices $\boldsymbol{x}_K$, $\boldsymbol{s}$, $\boldsymbol{y}_{\sigma_i}$, $\boldsymbol{y}_{e_i}$, $i = 1, \ldots, n$, where the faces and the edges of K having the vertex $\boldsymbol{s}$ are respectively σ_i and e_i, $i = 1, \ldots, n$ (in the general case, $n = 3$ for standard meshes); the set of the faces of this polyhedron is denoted by $\mathcal{F}_{K,\boldsymbol{s}}$; we denote, for all $\sigma \in \mathcal{F}_{K,\boldsymbol{s}}$, by $K_{\boldsymbol{s}}^\sigma$ the element of any partition of $K_{\boldsymbol{s}}$ such that

$$m_{K_{\boldsymbol{s}}^\sigma} = \frac{m_\sigma}{\sum_{\sigma' \in \mathcal{F}_{K,\boldsymbol{s}}} m_{\sigma'}} m_{K_{\boldsymbol{s}}}.$$

Then the scheme is defined by the method described by Eymard et al. (2009):

1. unknowns u_K are defined at the points $\boldsymbol{x}_K$ and u_σ at the points $\boldsymbol{x}_\sigma$, where σ is a face of any subcontrol volume $K_{\boldsymbol{s}}$;

2. if σ is a face of any subcontrol volume $K_{\boldsymbol{s}}$ such that σ is internal to K, then the value u_σ is expressed by a consistent linear combination of values u_K, due to consistent expressions at points $\boldsymbol{y}_\sigma$ and $\boldsymbol{y}_e$. If the point $\boldsymbol{y}_\sigma$ is not in the face σ, then σ is considered as a hybrid face and therefore u_σ becomes an additional unknown;

3. the discrete space $X_{\mathcal{D}}$ is defined as the set of all discrete unknowns $(u_K), (u_\sigma)$ respecting the Dirichlet boundary conditions and taking into account the hybrid unknowns;

4. the scheme consists in writing the discrete variational formulation

$$\text{Find } u \in X_{\mathcal{D}} \text{ such that } \int_\Omega \nabla_{\mathcal{T}} u(\boldsymbol{x}) \cdot \Lambda_{\mathcal{T}}(\boldsymbol{x}) \nabla_{\mathcal{T}} v(\boldsymbol{x}) \mathrm{d}\boldsymbol{x} = \int_\Omega f(\boldsymbol{x}) v(\boldsymbol{x}) \mathrm{d}\boldsymbol{x}, \ \forall v \in X_{\mathcal{D}}, \quad (8)$$

where $\Lambda_{\mathcal{T}}(\boldsymbol{x}) = \Lambda_K$ for $\boldsymbol{x} \in K$ and $\nabla_{\mathcal{T}} u(\boldsymbol{x}) = \nabla_{K,\boldsymbol{s}}^\sigma u$ for $\boldsymbol{x} \in K_{\boldsymbol{s}}^\sigma$ with

$$\nabla_{K,\boldsymbol{s}}^\sigma u = \nabla_{K,\boldsymbol{s}} u + \beta \frac{\sum_{\sigma' \in \mathcal{F}_{K,\boldsymbol{s}}} m_{\sigma'}}{m_{K_{\boldsymbol{s}}}} (u_\sigma - u_K - \nabla_{K,\boldsymbol{s}} u \cdot (\boldsymbol{y}_\sigma - \boldsymbol{x}_K)) n_{K_{\boldsymbol{s}},\sigma},$$

setting

$$m_{K_s} \nabla_{K,s} u = \sum_{\sigma \in \mathcal{F}_{K,s}} m_\sigma (u_\sigma - u_K) n_{K_s,\sigma},$$

and where $v(\boldsymbol{x})$ denotes a reconstruction at point $\boldsymbol{x}$ of an element $v \in X_{\mathcal{D}}$. In the above formula, β denotes a positive coefficient (the value 1 being chosen in practice).

This method leads to a new scheme with the following main characteristics

- it provides the exact solution if Λ is piecewise constant in polygonal sub-domains and u is affine in each of these sub-domains (this property is sought in the MPFA schemes);
- it leads to a 27-point scheme in the case of quadrilateral meshes which are not too distorted (in a sense involving the diffusion matrix Λ);
- it is a consistent, symmetric and convergent scheme for linear diffusion problems, such that a convergence proof can be given.

Comparison of the finite volume schemes for a deviated well single-phase analytical solution

Let us consider a straight line l_w in $\mathbb{R}^3$ and the cylinder Ω_w of radius r_w and of axis l_w. Let Λ be an anisotropic homogeneous permeability field assumed to be diagonal in the fixed Cartesian coordinates x, y, z. Its diagonal terms are denoted by λ_x, λ_y and λ_z.

An analytical solution P_e is built in Aavatsmark and Klausen (2003) for the single-phase Darcy flow on the domain $\mathbb{R}^3 \setminus \bar{\Omega}_w$ satisfying

$$-\nabla \cdot (\Lambda \nabla P_e) = 0 \text{ on } \mathbb{R}^3 \setminus \bar{\Omega}_w,$$

with an imposed pressure P_w and an imposed lineic flow rate Q_w at the well boundary $\partial\Omega_w$.

To define our bounded domain Ω, the infinite domain $\mathbb{R}^3 \setminus \Omega_w$ is cut by a bounded box aligned with the x, y, z coordinates of size L_x, L_y, L_z. A family of refined meshes is built on this domain as shown in Figure 1 with an exponentially refined radial mesh (Figure 1(a)) down to the well boundary and two types of transition meshes to connect this radial mesh to the outer boundary of the box. The radius of the radial zone is denoted by r_e and the transition mesh uses either hexahedra (unstructured hexahedral mesh (Figure 1(b))) or tetrahedra and pyramids (hybrid mesh (Figure 1(c))).

Let $\bar{P}_e$ be the restriction of P_e to Ω. It is the solution of the following single-phase Darcy flow with Dirichlet boundary conditions

$$\begin{cases} -\nabla \cdot (\Lambda \nabla \bar{P}_e) = 0 & \text{on } \Omega, \\ \bar{P}_e = P_e & \text{on } \partial\Omega. \end{cases} \tag{9}$$

This model problem and its analytical solution are used to study the convergence of the O, L, G, GradCell and SUSHI finite volume schemes. The errors are measured in the following discrete l^2 norm for the pressure approximate solution $P \in X_{\mathcal{T}}$

$$\| P - \bar{P}_e \|_{l^2}^2 = \frac{\sum_{K \in \mathcal{T}} m_K (P_K - \bar{P}_e(\boldsymbol{x}_K))^2}{\sum_{K \in \mathcal{T}} m_K}$$

where $\boldsymbol{x}_K$ is the center of gravity of the cell K. The errors are plotted as functions of the mesh size h, defined here by the diameter of the largest cell in the radial part of the mesh. The well axis l_w is deviated by θ_w degrees away from the vertical axis z in the x, z plane. Two anisotropy ratios for the permeability field are considered with $\lambda_x = \lambda_y$ and both $\lambda_z = \frac{\lambda_x}{5}$ and $\lambda_z = \frac{\lambda_x}{20}$.

In the experiments presented below we fix the following geometrical data:

- $L_x = 30$ m, $L_y = 30$ m et $L_z = 15$ m,
- $r_w = 10$ cm,
- $r_e = 5$ m,
- $\theta_w = 20$ degrees.

For the hybrid mesh family, the numerical convergence behavior is exhibited in Figure 5. Observe first that the error is the smallest with the O scheme for all cases. Its convergence rates are of order h^2 as it would be expected on the radial mesh. However, the main drawback of the O scheme on this type of mesh is its very large stencil. Therefore, it is also the most expensive in terms of computer memory and CPU time. The L scheme convergence is not plotted for the hybrid mesh family due to a failure

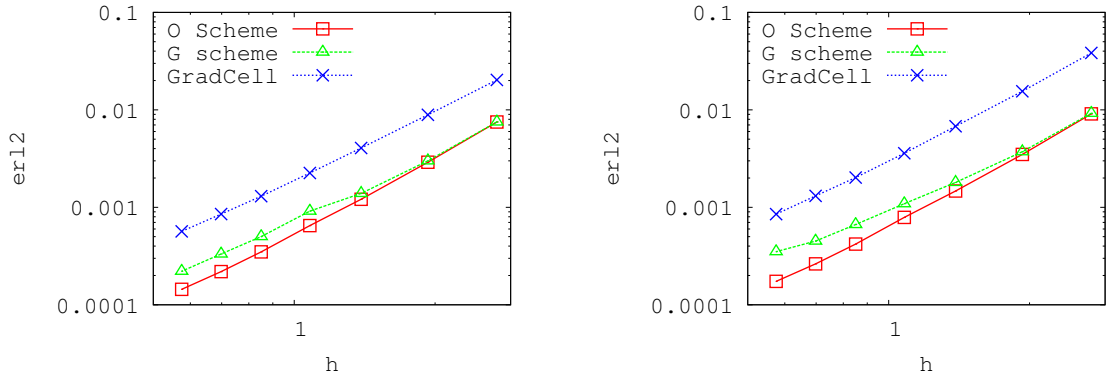

(a) anisotropy ratio 5 (b) anisotropy ratio 20

Figure 5 *l^2 pressure error function of h - hybrid mesh family*

in the construction of the numerical fluxes. Indeed, a few local matrices A^G (see (5)) for the gradient reconstruction are singular. The more flexible G scheme avoids this problem by not taking into account the groups G leading to singular matrices A^G in the linear combinations (7) defining the numerical fluxes. Using this trick, the results obtained by the G scheme are quite close to those of the O scheme, especially for coarse meshes.

Despite a quadratic convergence, the error of the GradCell scheme is clearly the largest in all cases. Nevertheless, compared to the O and G schemes, the GradCell scheme has the advantage that its stencil, as show in Table 6, is in average four times smaller and hence leads to a considerably reduced memory size and CPU time. Figure 7(a) even shows that, for a given l^2 error, the GradCell scheme is sparser and hence less expensive than the O scheme until the l^2 error reaches roughly 10^{-3}.

Note that the implementation of the SUSHI scheme, taking into account pyramids, is actually ongoing and related results will be presented in a future time.

	mesh 1	mesh 2	mesh 3	mesh 4	mesh 5	mesh 6	mesh 7
O and G schemes	130	139	112	104	101	105	106
GradCell scheme	28	28	28	28	28	28	28

Figure 6 *Stencil of O, G and GradCell schemes on hybrid meshes*

For the unstructured hexahedral mesh family, the numerical convergence behavior is exhibited in Figure 8. The rate of convergence is again of order h^2 for all schemes. The O and L schemes have the same behavior, their error plots are roughly speaking superposed. The SUSHI scheme provides the smaller

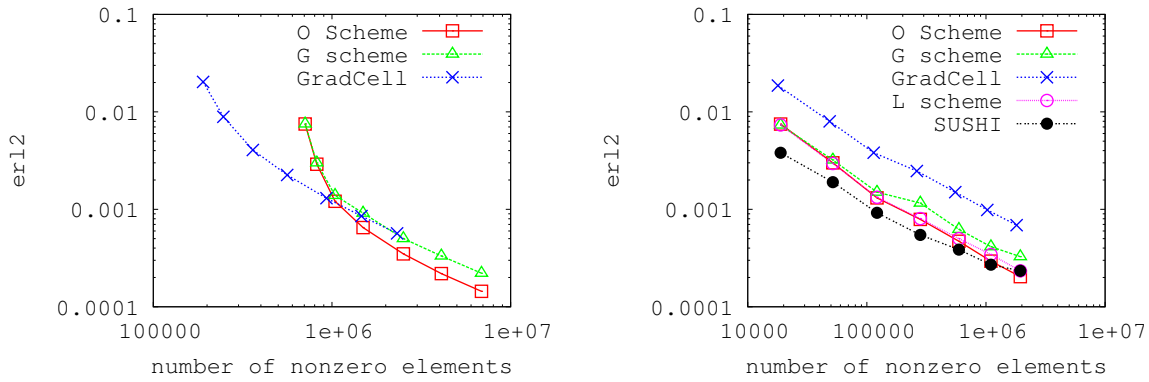

(a) hybrid meshes (b) hexaedral meshes

Figure 7 *l^2 pressure error function of nonzero elements in the linear system - anisotropy ratio 5*

error, particularly on coarse meshes. This can be explained by the fact that when we refine the mesh, we multiply our chance to obtain planar faces. Moreover, SUSHI defines the subcells such that their faces are triangular, so the scheme is less sensitive to non planarity than O and L schemes. Comparing the

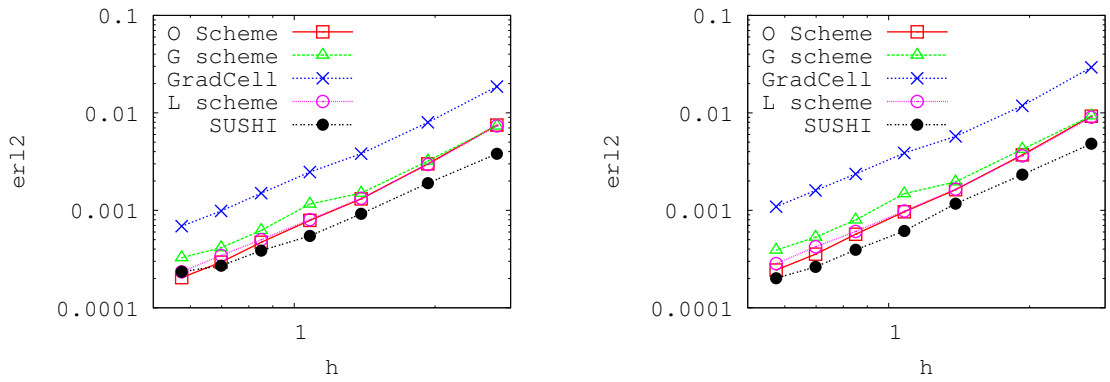

(a) anisotropy ratio 5 (b) anisotropy ratio 20

Figure 8 *l^2 pressure error function of h - unstructured hexahedral mesh family*

Figures 8(a) and 8(b), we see that SUSHI is more robust when the ratio of anisotropy increases. Table 9 shows that the number of hybrid unknowns introduced by the SUSHI scheme is negligeable compared to the number of the cell-centered unknowns.

The G and the GradCell schemes exhibit the same behavior here as for the hybrid mesh family. Indeed, the results obtained by the G scheme are quite close to the O and L schemes but its error in pressure is slightly larger. The GradCell scheme has again the largest error in all cases although its convergence rate is optimal. Its stencil is still smaller than the one of the O scheme but only slightly for this type of mesh.

	mesh 1	mesh 2	mesh 3	mesh 4	mesh 5	mesh 6	mesh 7
♯ control volumes	890	2232	5016	11220	23210	42633	74679
♯ hybrid edges	0	32	0	0	24	40	44

Figure 9 *Number of hybrid unknowns introduced by the SUSHI scheme.*

Finally, as expected, the numbers of nonzero elements in the linear system are similar for each scheme as can be infered from the comparison of Figures 7(b) and 8(a).

CO_2 injection two-phase Darcy flow near-well simulations

In this section, a two-component (H_2O and CO_2) two-phase (water and gas denoted respectively by w and g) Darcy flow is considered with solubility of the CO_2 component in the water phase. The media is as above anisotropic and homogeneous with diagonal permeability tensor in the x, y, z coordinates, and we consider an injection of CO_2 from the above deviated well into the reservoir saturated with water. The meshes are the same as in the previous section.

There is to our knowledge no analytical solution to this problem. Thus, this work focuses on two main issues, first the dependence of the solution on both families of meshes, and second the behavior of the non linear and linear solvers. In view of the results obtained in the single-phase case, the choice of the finite volume scheme is the O scheme which exhibits on both types of meshes a very good accuracy.

The model accounts for the following conservation equations of the two components

$$\begin{aligned}
H_2O \quad &: \quad \frac{\partial}{\partial t}\left(\phi \rho_w S_w C^w_{H_2O}\right) + \nabla \cdot \left[-\rho_w C^w_{H_2O} \frac{k_{r_w}(S_w)}{\mu_w} \Lambda(\nabla P - \rho_w \vec{g})\right] = 0, \\
CO_2 \quad &: \quad \frac{\partial}{\partial t}\left(\phi \rho_w S_w C^w_{CO_2} + \phi \rho_g S_g\right) \\
&\quad + \nabla \cdot \left[-\rho_w C^w_{CO_2} \frac{k_{r_w}(S_w)}{\mu_w} \Lambda(\nabla P - \rho_w \vec{g}) - \rho_g \frac{k_{r_g}(S_g)}{\mu_g} \Lambda(\nabla P - \rho_g \vec{g})\right] = 0,
\end{aligned}$$

where

- ϕ is the porosity with $\phi = 0.1$,
- $\vec{g}$ is the gravity with $\| \vec{g} \| = 10$ kg.m.s^{-2},
- C_i^α is the mass fraction of the component i in the phase α,
- S_α, ρ_α and μ_α are respectively the saturation, the density and the viscosity of the phase α, with $\rho_w = 1000$ kg.m^3, $\rho_g = 500$ kg.m^3, $\mu_w = 3.\ 10^{-4}$ Pa.s and $\mu_g = 3.\ 10^{-5}$ Pa.s,
- $k_{r_\alpha}(S_\alpha)$ is the relative permeability of the phase α defined here by $k_{r_\alpha}(S_\alpha) = S_\alpha$,
- Λ is still the diagonal permeability tensor. Here λ_x = λ_y = $1.\ 10^{-13}$ m^2 and $\lambda_z = \frac{\lambda_x}{10}$.

The problem is closed by the volume balance and the sum to one of the mass fractions

$$\begin{cases} S_w + S_g = 1, \\ C^w_{H_2O} + C^w_{CO_2} = 1, \end{cases}$$

as well as the thermodynamic equilibrium defined by the solubility $\bar{C}$ and the following complementary conditions

$$\begin{cases} (C^w_{CO_2} - \bar{C}) \leq 0, \quad S_g \geq 0, \\ (C^w_{CO_2} - \bar{C}) S_g = 0. \end{cases}$$

In the following experiments the solubility $\bar{C}$ is set to the constant value 0.05.

The CO_2 is injected from the deviated well in gaseous state inside the reservoir saturated with water of composition $C^w_{H_2O} = 1$. Homogeneous Neumann boundary conditions are set on the north and south sides for both phases and Dirichlet boundary conditions are set for all other sides. Hydrostatic pressure condition is imposed on the outer Dirichlet boundary and in the reservoir at the inital state

$$P(x, y, z) = P_1 \frac{L_x - x}{L_x} + P_2 \frac{x}{L_x} - \rho_w \| \vec{g} \| z,$$

with $P_1 = 240\ 10^{+5}$ Pa, $P_2 = P_1 - 1\ 10^{+4}$ Pa and $(x, y, z) \in [-15, 15] \times [-15, 15] \times [-7.5, 7.5]$. The initial saturations and compositions of the reservoir are those of pure water : $S_w = 1$ and $C^w_{\mathrm{H_2O}} = 1$. The input fluid at the outer Dirichlet boundary is also pure water.

To complete the description of the test case, hydrostatic pressure condition is also imposed at the well boundary

$$P(x, y, z) = P_{\text{well}} - \rho_g \parallel \vec{g} \parallel z,$$

with $P_{\text{well}} = 250\ 10^{+5}$ Pa. As mentioned above the injected fluid at the well boundary is pure gas : $S_g = 1$ and $C^w_{\mathrm{CO_2}} = 1$.

The model is discretized using a fully implicit Euler integration in time and a finite volume discretization in space. The Darcy fluxes are approximated using the O scheme, and the mobilities and concentrations at inner faces are upwinded with respect to the sign of the water and gas phase velocities.

Let α denote the water or gas phase. We consider in the subsequent discussion the following outputs function of time: first the rate of variation of the mass of CO_2 in the phase α inside the reservoir denoted by $\dot{m}^{\alpha}_{\mathrm{CO_2}}$, and second the outflowing mass flow rate of CO_2 in the phase α at the outer boundary denoted by $Q^{\alpha}_{\mathrm{CO_2}}$.

The final simulation time is fixed to 4 hours so that the gas phase has reached all sides of the external domain. In order to obtain a good convergence behavior in time, the time step is fixed to 150 seconds for both families of meshes.

The space convergence is preliminary studied as shown in Figure 10 for the output $\dot{m}^{\alpha}_{\mathrm{CO_2}}$ function of time. Once the gas front exits from the radial zone, we can notice that the convergence is much faster for the hybrid meshes due to a better accuracy of the upwind scheme for tetrahedral meshes than for hexahedral meshes. This remark will be further discussed below.

Next, the dependence of the solution on both types of meshes is studied using the finest hexahedral mesh 7 with 74679 cells and the finest hybrid mesh 6 with 77599 cells for which the solutions seem to have attained a good convergence.

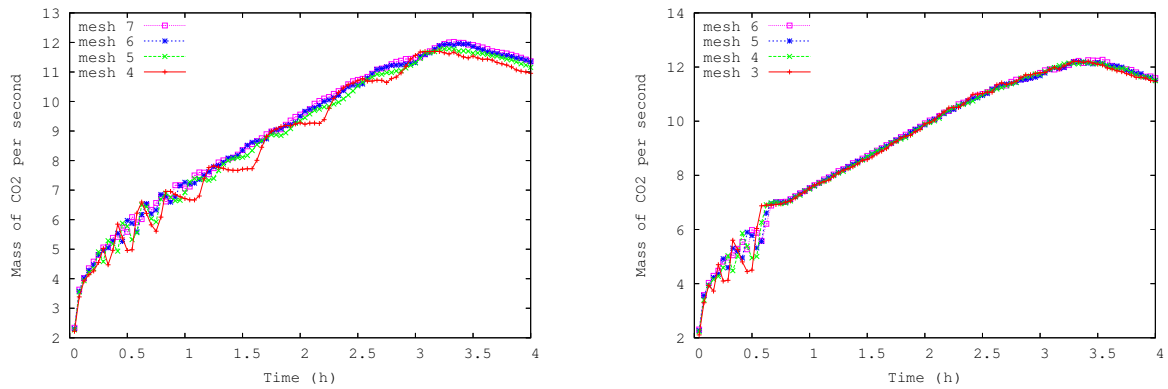

(a) hexahedral meshes

(b) hybrid meshes

Figure 10 *Convergence in space of the ouput* $\dot{m}^{g}_{co_2}$ *function of time.*

The histories of $\dot{m}^{\alpha}_{\mathrm{CO_2}}$, $\alpha = w, g$ are plotted for both types of meshes in Figure 11. Similarly, Figure 12 exhibits the histories of $Q^{\alpha}_{\mathrm{CO_2}}$ for $\alpha = w, g$.

Figures 11(a) and 11(b) clearly show that the solutions on both type of meshes begin to differ at the time $t_r \approx 0.65$ hours when the gas front exits from the radial mesh. From Figures 11(a) and 12, for $t > t_r$, the gas and water fronts seem to move faster in the hexahedral mesh than in the hybrid mesh. It

is confirmed by Figure 11(b) showing that between $t = t_r$ and $t = t_w \approx 2$ hours, CO_2 dissolves faster in the aquifer in the case of the hexahedral mesh than for the hybrid mesh. Here t_w denotes the time at which the water phase reaches the outer boundary. For $t > t_w$ this faster dissolution of CO_2 in the reservoir is balanced by the fact that the water phase outflows more rapidly at the outer boundary in the case of the hexahedral mesh.

This difference between the fronts for the two families of meshes may be explained by the so-called grid orientation effect (GOE). Let us recall that the GOE is a numerical instability due to the upstream discretization of the saturation equation appearing when adverse mobility ratios are used together with structured or quasi structured grids. The hexahedral mesh is clearly oriented in the axis directions and may suffer from the GOE effect leading to directional fronts while the more isotropic hybrid mesh leads to more isotropic fronts away from the radial zone.

The jump of the hybrid mesh solution in Figures 11(a) and 11(b) at $t = t_r$ can now be explained by the GOE effect which also takes place in the radial mesh whereas it is no longer the case in the tetrahedral mesh.

Note also that the oscillations exhibited in Figure 11(b) are a well known phenomenon due to the appearance of the gas phase in the successive cells when the CO_2 concentration reaches the solubility coefficient $\bar{C}$.

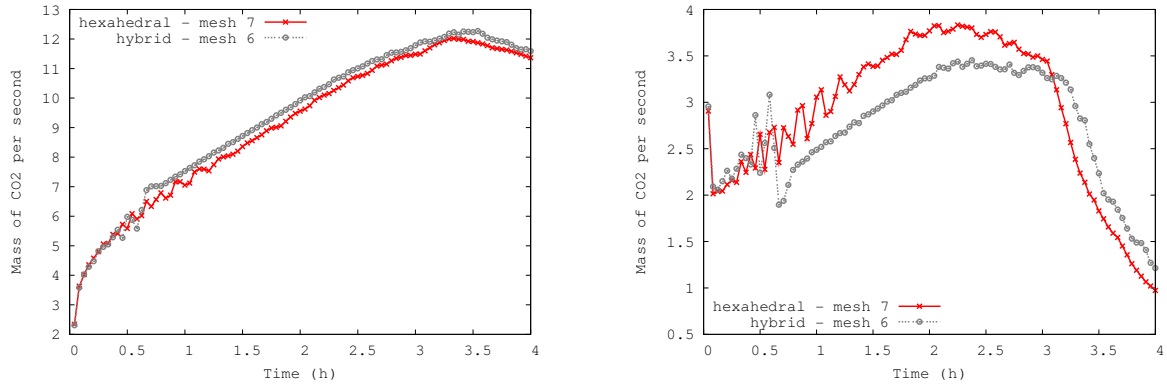

(a) CO_2 in gas phase

(b) CO_2 in water phase

Figure 11 *$\dot{m}^g_{co_2}$ and $\dot{m}^w_{co_2}$ function of time.*

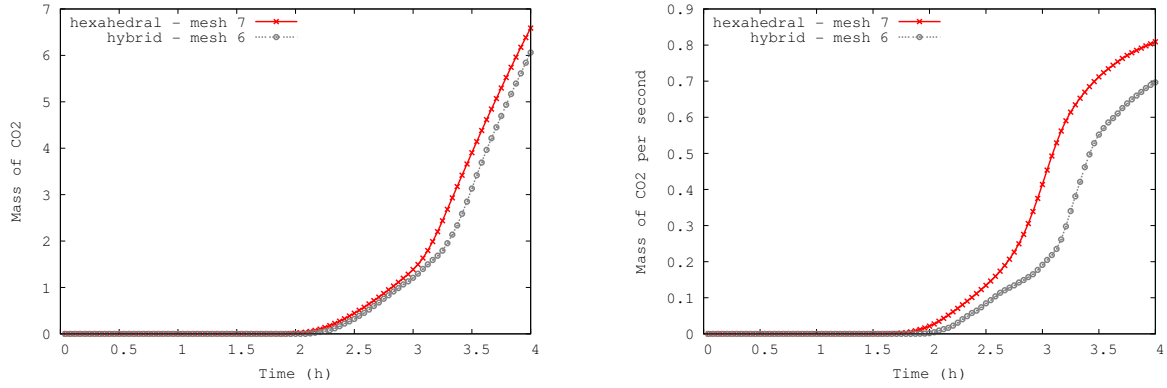

(a) CO_2 in gas phase

(b) CO_2 in water phase

Figure 12 *$Q^g_{co_2}$ and $Q^w_{co_2}$ function of time*

The behavior of the linear and non linear solvers are described in Table 14. A Newton non linear solver

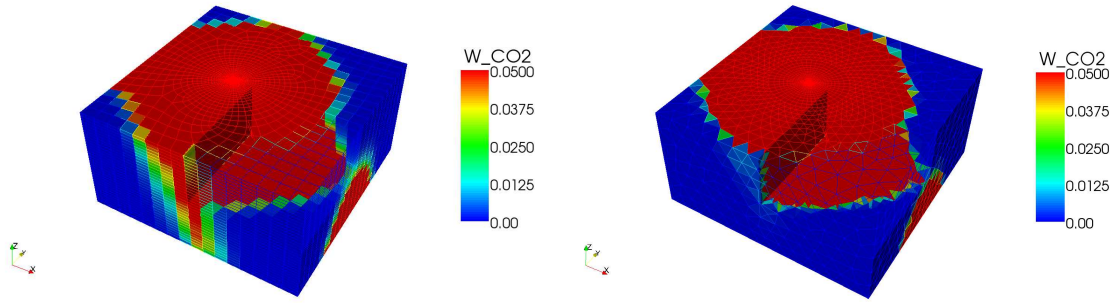

(a) hexahedral (b) hybrid

Figure 13 *Mass fraction of CO_2 dissolved in the water phase after 3 hours*

and a GMRES iterative solver preconditioned by CPR-AMG are used. It shows that the hexahedral meshes lead to fewer non linear and linear iterations as it could be expected from the better coercivity and monotonicity properties of the O scheme on this type of mesh for such an anisotropic media. This higher number of global linear iterations together with the larger stencil of the O scheme additionally increase the cost of hybrid meshes compared to hexahedral meshes.

	mesh 1	mesh 2	mesh 3	mesh 4	mesh 5	mesh 6	mesh 7
Newton	294	294	300	307	309	320	328
GMRES	2434	3145	3789	4613	5439	6457	6964

(a) hexahedral meshes

	mesh 1	mesh 2	mesh 3	mesh 4	mesh 5	mesh 6
Newton	343	349	354	359	371	380
GMRES	6097	6327	5340	5958	7223	8480

(b) hybrid meshes

Figure 14 *Total number of Newton and GMRES iterations for each meshes*

Conclusion

For single-phase flow, unstructured hexahedral near-well meshes lead to a reduction of memory size and CPU time for a given accuracy as well as an increased robustness. Note that, for a given radial zone, hybrid meshes lead to smaller l^2 errors on pressure. However, for an equivalent number of cells, the error is similar for both hybrid and hexahedral meshes whereas the cost is much higher for the hybrid meshes due to their larger stencils.

The MPFA O, L and G schemes perform all well for hexahedral meshes. The new SUSHI scheme exhibits very promising results, it is more accurate than the O scheme and should also be more robust due to its unconditional coercivity. The additional cost due to extra face unknowns is always negligible in our test cases.

In the case of hybrid meshes, the L scheme fails due to the singularity of a few local linear systems used to compute the gradients. The more flexible G scheme can circumvent this difficulty but it is still less accurate than the O scheme. The GradCell scheme is less accurate than the O and G schemes but its stencil is 4 times sparser which results for the coarsest meshes in a better accuracy for a given cost of the linear system solution.

Regarding the CO2 injection two-phase flow simulations, the hexahedral meshes still lead to a reduced memory size and CPU time compared to the hybrid meshes. Nevertheless, as opposed to the single-

phase case, we have noticed rather large differences between the converged solutions on both type of meshes due to the upwind scheme for the saturations and compositions. It seems that it can be explained by the Grid Orientation Effect (GOE) both in the radial mesh and in the hexahedral matching mesh. To check this assumption, further investigation is needed. We will first modify the mesh in the radial zone using a subdivision of each hexahedron into two prismatic cells. Second, in order to reduce the GOE effect on the hexahedral meshes, fluxes between cells sharing only a vertex can be introduced preserving the overall conservation of the fluxes in each cell.

References

Aavatsmark, I. [2002] An introduction to multipoint flux approximations for quadrilateral grids. *Comput. Geosci.*, **6**(3-4), 405–432, locally conservative numerical methods for flow in porous media.

Aavatsmark, I. [2007] Multipoint flux approximation methods for quadrilateral grids. *9th International Forum on Reservoir Simulation, Abu Dhabi*.

Aavatsmark, I., Eigestad, G., Heimsund, B., Mallison, B., Nordbotten, J. and Cian, E. [2007] A new finite-volume approach to efficient discretization on challenging grids. *SPE Reservoir Simulation Symposium*.

Aavatsmark, I., Eigestad, G., Mallison, B. and Nordbotten, J. [2008] A compact multipoint flux approximation method with improved robustness. *Numerical Methods for Partial Differential Equations*, **24**(5), 1329–1360.

Aavatsmark, I. and Klausen, R. [2003] Well index in reservoir simulation for slanted and slightly curved wells in 3d grids. *SPE Journal*, **8**(1), 41–48.

Agélas, L., Di Pietro, D. and Droniou, J. [2010a] The g method for heterogeneous anisotropic diffusion on general meshes. *M2AN Math. Model.Numer. Anal.*

Agélas, L., Di Pietro, D., Eymard, R. and Masson, R. [2010b] An abstract analysis framework for nonconforming approximations of anisotropic heterogeneous diffusion. *International Journal on Finite Volumes*, **7**(1), 1–29.

Agélas, L., Eymard, R. and Herbin, R. [2009] A nine-point finite volume scheme for the simulation of diffusion in heterogeneous media. *C. R. Math. Acad. Sci. Paris*, **347**(11-12), 673–676.

Agélas, L. and Masson, R. [2008] Convergence of the finite volume mpfa o scheme for heterogeneous anisotropic diffusion problems on general meshes. *Comptes Rendus Mathematique*, **346**(17-18), 1007–1012.

Edwards, M. [2002] Unstructured, control-volume distributed, full-tensor finite-volume schemes with flow based grids. *Computational Geosciences*, **6**(3), 433–452.

Edwards, M. and Rogers, C. [1998] Finite volume discretization with imposed flux continuity for the general tensor pressure equation. *Computational Geosciences*, **2**(4), 259–290.

Eymard, R., Gallouët, T. and Herbin, R. [2009] Discretisation of heterogeneous and anisotropic diffusion problems on general non-conforming meshes, sushi: a scheme using stabilisation and hybrid interfaces, to appear in IMAJNA, see also `http://hal.archives-ouvertes.fr/`.

Mundal, S., Keilegavlen, E. and Aavatsmark, I. [2008] Discretisation schemes for anisotropic heterogeneous problems on near-well grid. *Proceedings of the 11th European Conference on the Mathematics of Oil Recovery (ECMOR XI)*.

Mundal, S., Keilegavlen, E. and Aavatsmark, I. [2009] Simulation of anisotropic heterogeneous near-well flow using mpfa methods on flexible grids. *Computational Geosciences*.

Peaceman, D. [1978] Interpretation of well-block pressures in numerical reservoir simulation. *SPE Journal*, **18**(3), 183–194.

Peaceman, D. [1983] Interpretation of well-block pressures in numerical reservoir simulation with nonsquare grid blocks and anisotropic premeability. *SPE Journal*, **23**, 531–543.